

Vibration rejection for inertially stabilized double gimbal platform using acceleration feedforward

Martin Řezáč and Zdeněk Hurák

Abstract—The paper documents a computational design and an experimental verification of a vibration rejection scheme for an inertially stabilized platform mounted on a mobile base. The mechanical configuration of the platform is that of a standard double gimbal, which realizes a mass stabilization of the line of sight of an optoelectronic payload such as a camera an/or laser ranger finder. Nonideal static balancing of the payload gives rise to projection of the carrier vibrations onto a disturbing torque acting on the payload around the joint axes. This disturbance can be left for the existing inertial angular rate feedback to attenuate but a better solution can be devised. The cause of this disturbing torque—the linear acceleration of the carrier—can be measured, filtered and fed forward to the two direct drive motors. Experiments prove that significant vibration rejection is achieved with this feedforward compensation scheme.

I. INTRODUCTION

This paper reports on a successful application of a feedforward scheme for rejection of a disturbing torque for an inertially stabilized platform. Even though the lessons learnt from this case study might be of a general interest, the particular platform for which the control design was performed was an airborne double gimbal platform motorized by two DC direct drives and with the payload consisting of two cameras (RGB and IR) and a laser range-finder. The control task for such platforms is to keep the line of sight (optical axis) of the optical or optoelectronic payload still even in presence of some unwanted rotational motion of the carrier. Feedback stabilization schemes based on combination of the convenient mass stabilization concept and measurements of inertial angular rates were surveyed in [1], [2] and [3]. The authors participated in a development of a functional prototype of one such system in Fig. 1. Some reports on solutions of partial problems were given in [4], [5] and [6].

The key assumption for basic techniques of inertial line-of-sight stabilization is that the payload is perfectly balanced, that is, the gimbal axis goes through the center of gravity of the payload. Ideally, in a complete absence of friction in the joints, the payload remains in whichever orientation it is brought to. However, this is totally unrealistic. Even with a very careful mechanical design, perfect balancing cannot be achieved. Mechanical finetuning by attaching some extra pieces of material to the body of the payload does not solve the problem completely because the center of gravity can

This work was supported by the Ministry of Education of the Czech Republic within the project called Center for Applied Cybernetics (1M0567) and by Ministry of Industry and Trade of the Czech Republic within TIP FR-TII/265.

M. Řezáč and Z. Hurák are with Faculty of Electrical Engineering, Czech Technical University in Prague, Czech Republic rezac.martin@fel.cvut.cz

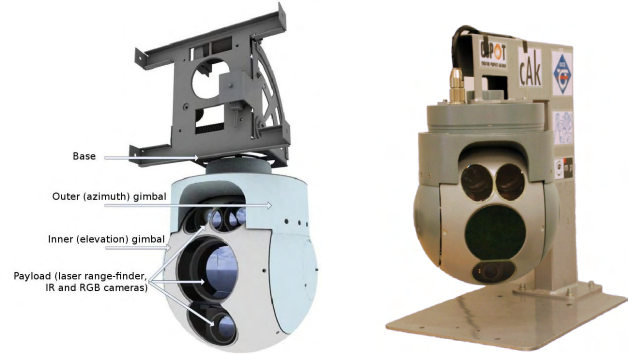


Fig. 1. Inertially stabilized camera platform developed by Czech Air Force and Air Defense Technological Institute in collaboration with Czech Technical University in Prague and ESSA company. The optical payload is supported by a double gimbal azimuth-elevation (Az-EI) system driven by two direct drive motors.

change during zooming. The geometry of the problem is sketched in Fig. 2 for a single axis of rotation orthogonal to the direction of acceleration.

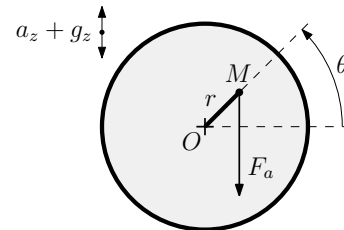


Fig. 2. Geometry of the problem for a single rotational axis perpendicular to the direction of the acceleration. If the case of an elevation joint in the azimuth-elevation (Az-EI) double gimbal system this is composed of both the gravitational and the translational acceleration.

Even if the carrier (base) of the double gimbal platform resides still on the ground, the static mass unbalance leads to a periodic disturbing torque acting on the payload added to the torque exerted by the direct drive motors. This is demonstrated using experimental data in Fig. 3. While the control system keeps the inertial angular rate constant, the voltage applied to the motor armature winding exhibits a periodic pattern. This reveals that the inertial angular rate control system motor has to cope with a periodic disturbance.

The situation is even worse when the carrier is exposed to a linear acceleration. This is the case when the platform is attached to a helicopter (as in Fig. 4). The unavoidable vibrations of the helicopter are passed to the platform and give rise to a more pronounced disturbing torque.

The situation for one rotational degree of freedom is

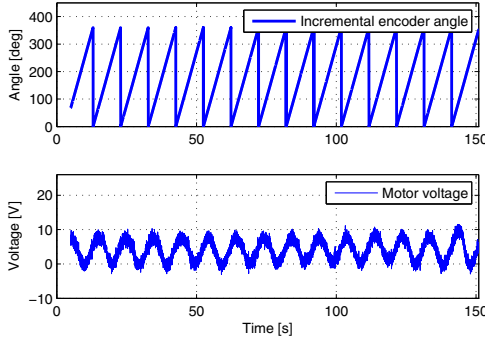


Fig. 3. Periodic pattern observed in the control voltage as a consequence of projection of a gravity onto a disturbing torque for a statically unbalanced elevation gimbal seated on the ground. The control system kept the inertial angular rate at some constant value.



Fig. 4. The inertially stabilized airborne camera platform attached to a helicopter has to withstand significant vibrations caused by the carrier.

modeled using a block diagram in Fig.5. The model includes all the necessary components for a one-axis motion control system driven by a DC motor, including a model of a friction. It makes it clear how the translational acceleration projects into a disturbing torque.

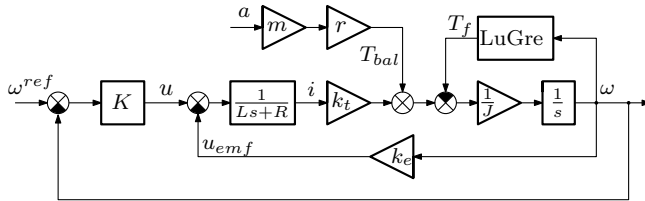


Fig. 5. Block diagram of the feedback setup with the entry point of the disturbance.

This disturbing torque can be left for the existing inertial angular rate feedback to reject but great advantage can be taken from the often neglected feedforward compensation. The cause of the disturbing torque—the linear acceleration of the carrier—can be measured, filtered and fed forward to the two direct drive motors. This technique of acceleration feedforward is often used in the domain of hard disk drives, see [7] [8] [9], but has not been described in the area of inertial stabilization.

The paper includes an analysis for the single axis case and uses experiments to prove that significant vibration rejection performance is achieved with this compensation scheme.

II. INERTIALLY STABILIZED DOUBLE-GIMBAL PLATFORM

The compensation scheme described in this paper is based on a mathematical model, therefore, a model is provided here for the considered benchmark system. Even though the full model should include gyroscopic interactions between the two axis, for practical purposes this is often neglected and each axis is control independently, treating the gyroscopic moments as yet another disturbance. The angular rates achievable by this type of systems are usually rather low, which justifies this simplification. A single axis situation is therefore modeled. The model is fairly standard and is included here for an easy reproducibility of the results.

A. Coordinate frames and rotation matrices

The paper relies on expressing rotations of coordinate frames with respect to some other coordinate frames. The right-handed orthogonal coordinate frames are represented by triads of vectors $\{x, y, z\}$ and for (justifiable) simplicity they all assume a common origin. The coordinate frames and their symbols used in subscripts and superscripts are: the base coordinate frame fixed to the body of the carrier [B] with its x_B axis heading forward and y_B to the starboard; the coordinate frame attached to the outer (azimuth) gimbal [A], which can rotate with respect to the carrier around the $z_B = z_A$ axis and finally the coordinate frame attached to the inner (elevation) gimbal [E], which can rotate with respect to the azimuth gimbal around the $y_A = y_E$ axis.

The sequence of rotations expressing the pose of the inner gimbal with respect to the base (carrier) is visualized in Fig. 6 and is analytically expressed as

$$R_B^A = \begin{bmatrix} \cos \psi & \sin \psi & 0 \\ -\sin \psi & \cos \psi & 0 \\ 0 & 0 & 1 \end{bmatrix}, \quad (1)$$

where the lower and upper indices are used here as "rotation matrix expressing the coordinate triad of the A frame within B frame" and

$$R_A^E = \begin{bmatrix} \cos \theta & 0 & -\sin \theta \\ 0 & 1 & 0 \\ \sin \theta & 0 & \cos \theta \end{bmatrix}. \quad (2)$$

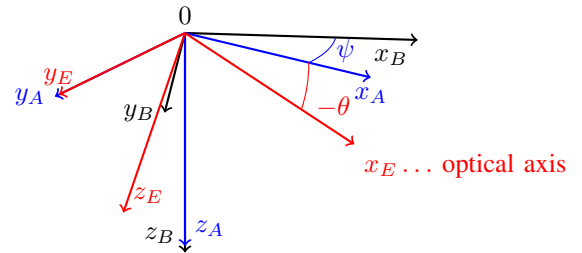


Fig. 6. Composition of rotation of coordinate frames attached to the carrier – base [B], azimuth gimbal [A] and inner (elevation) gimbal [E].

The right-hand rule set the orientation of the angular rotations such that the outer (azimuth) gimbal rotates to

right for positive ψ and the inner (elevation) gimbal rotates upwards for a positive increment in θ . Using the common shorthand notation like $c_\psi = \cos \psi$, the composition of the two rotations is given by the matrix product

$$R_B^E = R_A^E R_B^A = \begin{bmatrix} c_\psi c_\theta & c_\theta s_\psi & -s_\theta \\ -s_\psi & c_\psi & 0 \\ c_\psi s_\theta & s_\psi s_\theta & c_\theta \end{bmatrix}. \quad (3)$$

The transposition of the above matrices give transformation in the opposite directions, that is $R_B^A = (R_A^B)^T$ can be used to transform the vector from the base frame to the outer gimbal frame (elevation) and so on.

Using these transformation matrices, the acceleration experienced by the gimbal base a_B (identical with the carrier) is projected to the outer (azimuth) gimbal as

$$a_A = R_B^A a_B \quad (4)$$

and to the inner (elevation) gimbal as

$$a_E = R_B^E a_B. \quad (5)$$

The acceleration a_E of the center of gravity of the inner gimbal generates a disturbing torque around the elevation y-axis in the camera body frame

$$T_{Ey} = [r_E \times m_E a_E]_y, \quad (6)$$

where r_E is a displacement vector of the center of mass and m_E is the mass of the inner gimbal, including the payload.

Similarly, the acceleration a_A generates the disturbing torque T_{Az} around the outer (azimuth) gimbal axis. But now it is comprised of two components

$$T_{Az} = [r_A \times m_A a_A]_z + [r_{EA}(\theta) \times m_E a_A]_z, \quad (7)$$

where the first component is the unbalance of the azimuth gimbal described by the mass m_A and the vector r_A , and the second component represents the unbalance of the elevation gimbal described by the mass m_E and the distance from the elevation gimbal center of mass to the azimuth joint axis (vector r_{EA} depending on the elevation angle $\theta(t)$).

B. Rigid body dynamics modeling

Both the elevation and the azimuth gimbals are modeled as a classical DC motor with a load¹. The standard *mechanical equation* of the DC motor attached via rigid link to load is

$$J\dot{\omega}(t) = k_t i(t) + T_{bal}(t) - T_f(t), \quad (8)$$

where $\omega(t)$ [rad/s] is the angular rate, $i(t)$ [A] is the motor current and $T_{bal}(t)$ [Nm] is the disturbing torque coming from gimbal unbalance (T_{bal} stands for either T_{Az} or T_{Ey}) and $T_f(t)$ stands for a frictional torque. The remaining parameters are listed in Table I. The *electrical equation* is

$$L \frac{di(t)}{dt} + Ri(t) + k_e \omega(t) = u(t), \quad (9)$$

¹The load for the azimuth axis depends on the elevation of the camera.

TABLE I
PARAMETERS OF THE ELEVATION GIMBAL (INCLUDING FRICTION)

Parameter	Value	Unit
Peak torque	$T_p = 0.42$	[N-m]
Supply voltage	$V_p = 26.0$	[V]
Motor torque constant	$k_t = 0.284$	[N-m/A]
Back e.m.f. constant	$k_e = 0.284$	[V/rad/s]
Armature resistance	$R = 16.5$	[Ohm]
Armature inductance	$L = 6.3$	[mH]
Moment of inertia	$J = 0.0455$	[kg-m/s ²]
Coulomb friction torque	$T_c = 0.03$	[N-m]
Stribeck friction torque	$T_s = 0.0664$	[N-m]
Stribeck velocity	$\omega_s = 0.05$	[rad/s]
Sigma 0	$\sigma_0 = 328$	[-]
Sigma 1	$\sigma_1 = 2.97$	[-]
Sigma 2 (viscous friction)	$\sigma_2 = 0.0644$	[N-m/rad/s]

where $u(t)$ is the voltage produced by the controller. Block diagrams are in Fig. 5.

C. Friction modeling

It appears in the experiments that friction in the joints plays a major role in determining the dynamic response of the platform. The need of a more advanced friction modeling and compensation is pronounced here because in a standard mode of use the system works in close neighborhood of a zero velocity operating point. Simple viscous or Coulomb friction models are not much useful. The popular LuGre dynamic friction model [10] was used here because it is capable of describing the frictional phenomena around zero velocity (Stribeck effect). A short introduction to LuGre model is made here just for convenience of readers. The dissertation theses [11], [12] and [13] may be used to get the insight to friction modeling, identification and estimation. Some more recent survey papers are [14], [15] and [16].

The LuGre model contains a single friction state $z(t)$ governed by

$$\dot{z}(t) = \omega(t) - \frac{|\omega(t)|}{g(\omega(t))} z(t), \quad (10)$$

where $g(\omega)$ is defined as

$$g(\omega) = \frac{1}{\sigma_0} \cdot \left(T_c + (T_s - T_c) e^{-(\omega(t)/\omega_s)^2} \right). \quad (11)$$

The friction torque $T_f(t)$ is then written as

$$T_f(t) = \sigma_0 z(t) + \sigma_1 \dot{z}(t) + \sigma_2 \omega(t). \quad (12)$$

Steady state characteristic of the friction model is

$$T_f(t) = T_c \text{sgn}(\omega(t)) + (T_s - T_c) \text{sgn}(\omega(t)) e^{-(\frac{\omega(t)}{\omega_s})^2} + \sigma_2 \omega(t). \quad (13)$$

For simulation purposes, all parameters of the model of the elevation gimbal (8) – (11) were identified and listed in Table I. Some parameters were known from the components' documentation, the remaining were identified using gray-box model fitting methods available in System Identification Toolbox for Matlab. The static part of the identified friction model is plotted in Fig. 7.

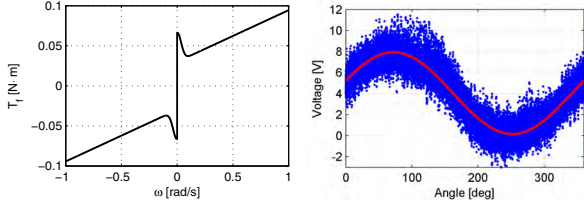


Fig. 7. Left: Static friction characteristic – the friction torque as a function of the angular velocity. Generated using (13) with the parameters in Table I. Right: The result of an experimental identification of a static mass unbalance. Fitting the sine wave is described by (17). The sum of sine and cosine results in a shifted sine. The blue color represents the data of several turns of the elevation gimbal. The red line represents the result of the fitting.

D. Experimental identification of elevation unbalance

In this section we assume that the (inertial) angular rate controller K from Fig. 2 is designed and fully working. It can track the reference angular rate ω^{ref} up to some reasonably high frequency (velocity loop bandwidth). The controller achieves this by measuring the angular rate ω using MEMS inertial angular rate sensors and setting the control voltage u . Within this setting, when the constant reference angular rate ω^{ref} is required, the control voltage u should be constant (in steady state). Nevertheless, the control voltage observed during this experiment clearly contains a sinusoidal content (see Fig. 3 or Fig. 8 on the left). This content corresponds to the gimbal unbalance since it is obviously dependent on the joint angle. Plotting the data from the Fig. 3 as the voltage u being a function of the gimbal angle θ gives Fig. 7. This sine wave originates from (6) with $a_B = [0 \ 0 \ g]^T$ as follows

$$T_{Ey} = \left[r_E \times (m_E R_B^E [0 \ 0 \ g]^T) \right]_y \quad (14)$$

$$= -m_E g (r_{Ez} \sin \theta + r_{Ex} \cos \theta) \quad (15)$$

$$= \bar{A} \sin \theta + \bar{B} \cos \theta. \quad (16)$$

In fact, it is not required to know the vector r_E and the mass m_E separately. The parameters \bar{A} and \bar{B} fully describe the torque necessary to reject the disturbance coming from static mass unbalance scaled by the gravity. To compensate not only for the gravity but also for a nonzero translational acceleration a_B , the acceleration measurement must be related to the gravity. It is not even necessary to estimate the parameters \bar{A} and \bar{B} relating the gimbal angle and the disturbing torque, but instead the parameters A and B relating the angle and the voltage necessary to reject the disturbance

$$u(\theta) = A \sin \theta + B \cos \theta + C. \quad (17)$$

The parameter C represents the constant voltage level required to reject friction torque. The parameters A and B are defined by

$$A = -m_E \cdot g \cdot r_{Ez} \cdot \frac{k_t}{R}, \quad (18)$$

$$B = -m_E \cdot g \cdot r_{Ex} \cdot \frac{k_t}{R}. \quad (19)$$

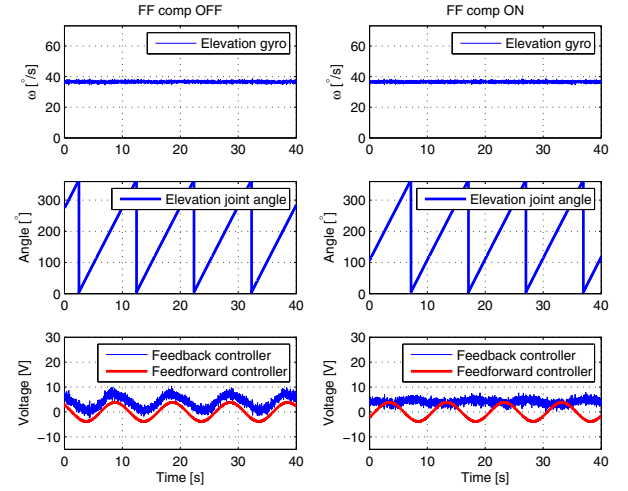


Fig. 8. The identification experiment showing the impact of a limited accuracy of the static mass unbalance identification. The elevation gimbal is rotating at a constant speed by a rate controller. On the left: the unbalance is clearly visible in the feedback controller's voltage (the feedforward red sine curve is plotted here too but it is not applied). On the right: the identified sine is added to feedback controller's output. Ideally, only friction force should be left for the feedback to compensate. In reality, the control voltage is not perfectly constant, which reveals that the feedforward did not reject the disturbance completely.

To estimate the parameters A , B and C , the least squares fitting was used since (17) is linear in these parameters. The resulting fit is visualized in Fig. 7.

III. FEEDFORWARD DISTURBANCE REJECTION

With a successfully identified and validated model of dynamics of the elevation gimbal, including the static mass unbalance, a feedforward disturbance rejection scheme based on measured acceleration may be devised. As discussed in the previous sections, an accelerometer is used to measure the vibrations.

A key decision is where to place the accelerometer. One possible choice is to place the sensor inside the elevation gimbal, fix it to the payload. This way, the values of a_{Ex} and a_{Ez} are measured directly. A major disadvantage of this choice is that the sensor must be placed exactly to the elevation joint axis otherwise its signal is distorted by the centripetal acceleration during the elevation gimbal rotations.

Another possibility (the one chosen in the paper) is to attach the accelerometer to the base, thus measuring a_B . The acceleration of the elevation gimbal a_E must be computed. The situation is depicted in Fig. 9. The feedforward controller F is using the accelerometer signal a_B and feeds it forward as a voltage u_{ff} applied to the elevation motor (in addition to the feedback controller voltage u_{fb}).

Looking at the Fig. 9, the key idea for design of a feedforward controller F is to achieve the transfer function from a_B to T identical to the transfer function from a_B to T_{Ey} . (The voltage u_{ff} is the outcome of the feedforward controller and not the torque). Using the identified parameters A and B this

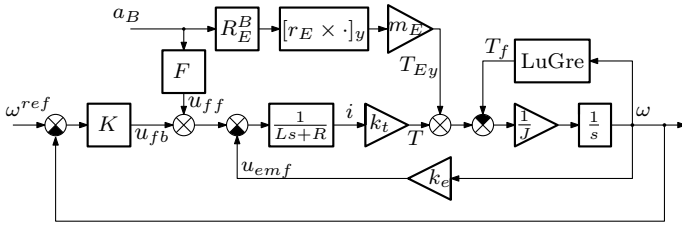


Fig. 9. Block diagram of the feedback setup with added feedforward controller F .

is satisfied by the controller with the transfer function

$$F = \frac{1}{g} \cdot \left(\frac{L}{R}s + 1 \right) \cdot \left[[B \ 0 \ A] \times R_E^B a_B \right]_y, \quad (20)$$

which is, however, not proper due to the motor inductance L . An additional low-pass filter must be added or the motor electrical dynamics may be neglected to obtain the reduced version of the controller in the form

$$F = \frac{1}{g} \cdot \left[[B \ 0 \ A] \times R_E^B a_B \right]_y. \quad (21)$$

The second variant may be easily justified in the case when the sampling rate of the control loop is $f_s = 200$ Hz, which is ten times lower than the frequency R/L .

A challenge in this type of feedforward disturbance rejection lies in the limited accuracy of the identified model, including the static mass unbalance. Possibly the dynamics of the accelerometer can not be neglected. The voltage u_{ff} produced by the feedforward controller F then does not reject the disturbance completely, as seen in the experimental data in Fig. 8. This calls for implementation of some adaptation.

IV. SIMULATIONS

To assist in designing the feedforward compensator, numerical simulations using Matlab/Simulink were used (see the model scheme in Fig. 11). Feedback loop was always closed. The new feedforward control always acted as a complement to the MEMS gyro based feedback control. The input to the simulations is the constant speed rotation of the elevation joint with simultaneously applied sinusoidal vertical vibrations a_{Bz} of amplitude 8 ms^{-2} . The frequency of the vibrations was linearly changing from 0.1 Hz to 10 Hz. In Fig. 10 the results of the simulation without applied feedforward controller are shown, followed by Fig. 10 with the simulation where the feedforward controller F from equation (21) was switched on.

V. EXPERIMENTAL RESULTS

Experimental verification was done using a professional laboratory vibration table (see Fig.12). The table allows for vertical motion with the frequency ranging from one to several tens of Hz with the amplitude of several centimeters. The experiment results are shown in Fig. 13 with the detail in Fig. 14. Consistently with the simulations, the reduced version of the feedforward controller (21) was implemented. Experimental results clearly confirm the usefulness of the

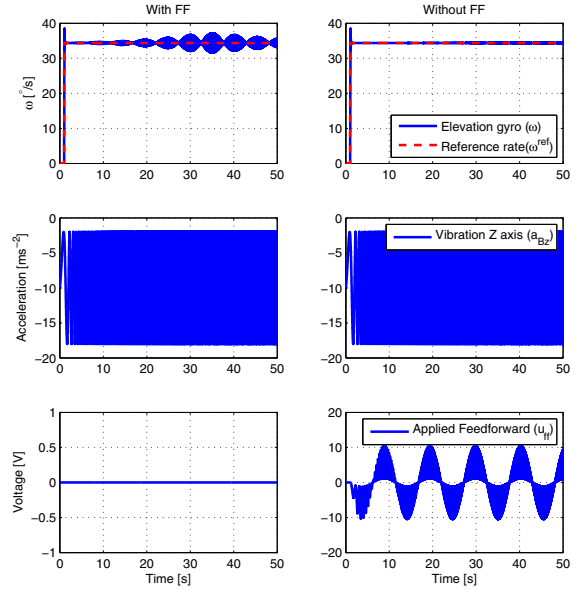


Fig. 10. Left: Simulation with the Feedforward controller switched OFF. The vibrations passing into the gyro signal are clearly visible here. The amplitude of vibrations passing into ω is changing in accordance with the projection R_E^B as the joint is rotating constant speed. Right: Simulation with the Feedforward controller switched ON. The angular gyro rate signal is here not disturbed by vibrations at all.

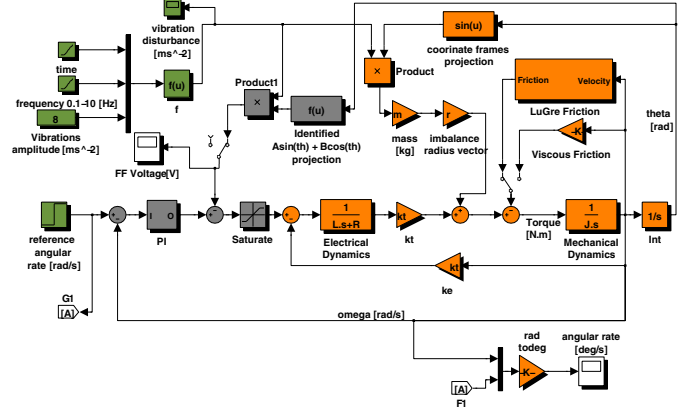


Fig. 11. Simulink model demonstrating the feedforward controller structure. The elevation joint model with the friction and imbalance is depicted by orange, dark green represents the input signals (ω_{ref} and a_B) and grey are the couple of feedforward and feedback controller.

feedforward compensator, even in its reduced form with the accelerometer sensor dynamics neglected.

VI. CONCLUSION

The paper reported on some early achievements with accelerometer-based feedforward vibration rejection for inertially stabilized double gimbal Az-El platform. It is suggested to decompose the problem into two independent problems, one for each gimbal (rotational axis). This report only handled the easy subproblem—the inner (elevation) gimbal. The outer (azimuth) gimbal brings about one major complication in that the relative displacement of the center of gravity with respect to the azimuth (vertical) rotational axis changes with the elevation angle of the inner gimbal and the intuitive



Fig. 12. The inertially stabilized platform placed on a vibration table.

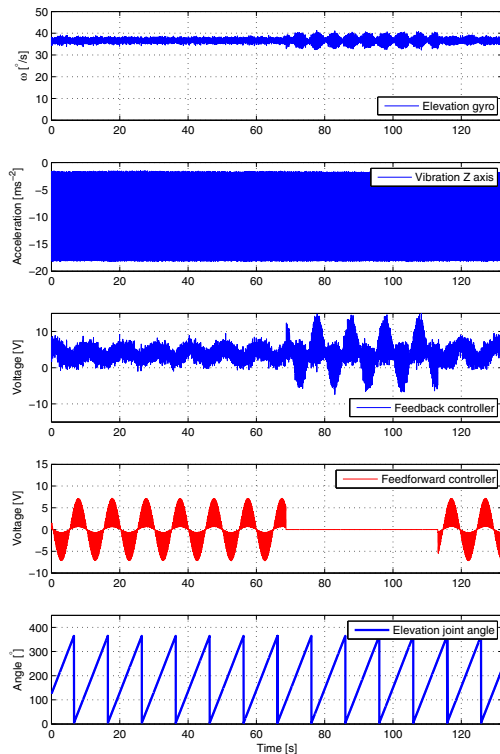


Fig. 13. Comparison of feedforward controller turned on and off during the experiment on the vibrational platform. See the feedforward controller signal to see when it is turned on and off.

unbalance identification method described in section II-D cannot be used for azimuth joint. Nonetheless, even the simple solution proposed in the paper proved functioning and useful in experiments with a real platform.

REFERENCES

- [1] M. Masten, "Inertially stabilized platforms for optical imaging systems: Tracking dynamic dynamic targets with mobile sensors," *Control Systems Magazine, IEEE*, vol. 28, pp. 47–64, Feb. 2008.
- [2] J. M. Hilker, "Inertially stabilized platform technology: concepts and principles," *Control Systems Magazine, IEEE*, vol. 28, pp. 26–46, Feb. 2008.
- [3] J. Debruijn, "Control systems for mobile satcom antennas," *Control Systems Magazine, IEEE*, vol. 28, pp. 86–101, 2008.
- [4] Z. Hurák and M. Režáč, "Combined line-of-sight inertial stabilization and visual tracking: application to an airborne camera platform," in *Proceedings of the 48th IEEE Conference on Decision and Control*, Shanghai, China, December 2009.

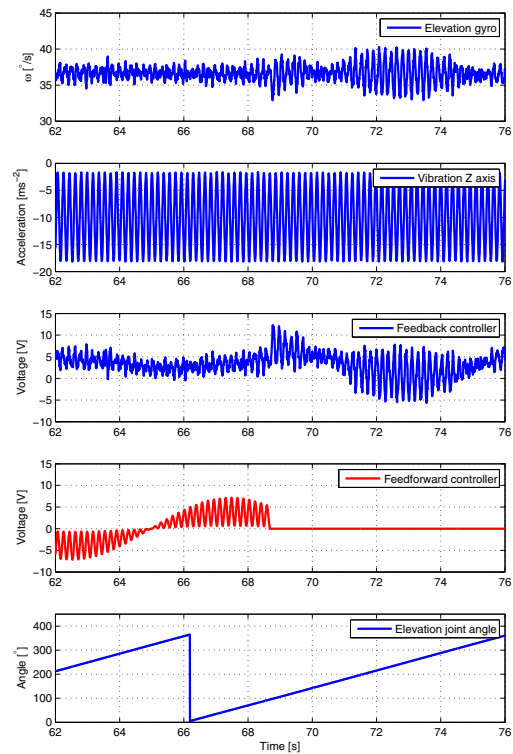


Fig. 14. Detail of the Fig. 13. Comparison of feedforward controller turned on and off during the experiment on the vibrational platform.

- [5] —, "Delay compensation in a dual-rate cascade visual servomechanism," in *Proceedings of the 49th IEEE Conference on Decision and Control*, Atlanta, GA, USA, December 2010.
- [6] —, "Control design for image tracking with an inertially stabilized airborne camera platform," in *Proceedings of SPIE Defence, Security, and Sensing 2010*, Orlando, Florida, USA, 2010.
- [7] C. S. Chen and Y. T. Teng, "Multirate digital servo drive based on acceleration observer and disturbance compensator," in *Proceedings of the 18th IFAC World Congress*, 2008, pp. 9278–9283.
- [8] S. Pannu and R. Horowitz, "Adaptive accelerometer feedforward servo for disk drives," in *Proceedings of the 36th IEEE Conference on Decision and Control*, vol. 5, 1997, pp. 4216–4218 vol.5.
- [9] M. T. White and M. Tomizuka, "Increased disturbance rejection in magnetic disk drives by acceleration feedforward control and parameter adaptation," *Control Engineering Practice*, vol. 5, no. 6, pp. 741–751, June 1997.
- [10] C. de Wit, H. Olsson, K. J. Åström, and P. Lischinsky, "A new model for control of systems with friction," *IEEE Transactions on automatic control*, vol. 40, no. 3, pp. 419–425, 1995.
- [11] F. Altpeter, "Friction modeling, identification and compensation," Ph.D. dissertation, École Polytechnique Fédérale de Lausanne, 1999.
- [12] H. Olsson, K. J. Åström, C. C. D. Wit, M. Gäfvert, and P. Lischinsky, "Friction models and friction compensation," *European Journal of Control*, vol. 4, pp. 176–195, 1998.
- [13] R. Hensen, "Controlled mechanical systems with friction," Ph.D. dissertation, Technische Universiteit Eindhoven (TU/e), 2002.
- [14] F. Al-Bender and J. Swevers, "Characterization of friction force dynamics," *Control Systems Magazine, IEEE*, vol. 28, no. 6, pp. 64–81, 2008.
- [15] K. Åström and C. Canudas-de-Wit, "Revisiting the LuGre friction model," *Control Systems Magazine, IEEE*, vol. 28, no. 6, pp. 101–114, 2008.
- [16] A. Harnoy, B. Friedland, and S. Cohn, "Modeling and measuring friction effects," *Control Systems Magazine, IEEE*, vol. 28, no. 6, pp. 82–91, 2008.